

# Anomalous ferromagnetism and magneto-optical Kerr effect in semiconducting double perovskite $\text{Ba}_2\text{NiOsO}_6$ and its (111) $(\text{Ba}_2\text{NiOsO}_6)/(\text{BaTiO}_3)_{10}$ superlattice

Hai-Shuang Lu<sup>1,2,3</sup> and Guang-Yu Guo<sup>1,3,\*</sup>

<sup>1</sup>*Department of Physics and Center for Theoretical Physics,  
National Taiwan University, Taipei 10617, Taiwan*

<sup>2</sup>*College of Physics and Electronic Engineering, Changshu Institute of Technology, Changshu 215500, People's Republic of China*

<sup>3</sup>*Physics Division, National Center for Theoretical Sciences, Hsinchu 30013, Taiwan*

(Dated: January 25, 2022)

We carry out a first-principles investigation on magnetism, electronic structure, magneto-optical effects and topological property of newly grown cubic double perovskite  $\text{Ba}_2\text{NiOsO}_6$  and its (111)  $(\text{Ba}_2\text{NiOsO}_6)/(\text{BaTiO}_3)_{10}$  superlattice, based on the density functional theory with the generalized gradient approximation (GGA) plus onsite Coulomb interactions. Interestingly, we find that both structures are rare ferromagnetic (FM) semiconductors with estimated Curie temperatures of  $\sim 150$  and  $70$  K, respectively. The calculated near-neighbor exchange coupling parameters reveal that the ferromagnetism is driven by exotic FM coupling between Ni and Os atoms, which is due to the FM superexchange interaction caused by the abnormally strong hybridization between the half-filled Ni  $e_g$  and unoccupied Os  $e_g$  orbitals. The strong spin-orbit coupling (SOC) on the Os atom is found to not only open the semiconducting gap but also produce a large antiparallel orbital magnetic moment on the Os atom, thus reducing the total magnetization from  $4.0 \mu_B/\text{f.u.}$ , expected from the  $\text{Ni}^{2+} 3d^8 (t_{2g}^6 e_g^2; S = 1)$  and  $\text{Os}^{6+} 5d^2 (t_{2g}^2 e_g^0; S = 1)$  ions. Remarkably, we also find that because of the enhanced exchange interaction on the Os atoms caused by the Ni  $3d$  - Os  $5d$  hybridization and the strong SOC of the Os atoms, the magneto-optical (MO) effects are large in these two structures. For example, the Kerr and Faraday rotations in bulk  $\text{Ba}_2\text{NiOsO}_6$  can be reach  $6^\circ$  and  $250 \text{ deg}/\mu\text{m}$ , respectively, which are larger than that of best-known MO materials. These interesting findings thus suggest that because of their FM semiconductivity and excellent MO properties, both structures would be promising materials for not only semiconductor-based spintronics but also magneto-optical devices. Finally, our calculated anomalous Hall conductivity shows that the band gap just below the Fermi level in the superlattice is topologically nontrivial with the gap Chern number of 2. This indicates that the (111)  $\text{Ba}_2\text{NiOsO}_6$  and related  $5d$  double-perovskite monolayers may provide an interesting material platform for exploring magnetic topological phases and phase transitions.

## I. INTRODUCTION

Double perovskite oxides  $\text{A}_2\text{BB}'\text{O}_6$  (A is a rare-earth/alkaline-earth cation; B and B' are transition metal cations), discovered in 1960s [1], have attracted enormous attention in the past decades. They have been found to show diverse properties, such as large room-temperature magnetoresistance [2], multiferroicity [3], half-metallicity [2, 4, 5], and magneto-optic (MO) effects [6, 7], depending on the compositions of the A, B, and B' cations. More recently, monolayers and multilayers of these double perovskites containing heavy cations were predicted to host various topological insulating phases such as quantum anomalous Hall phase [8–11]. Therefore, double perovskite oxides offer ample possibilities for exploration of spin-related physics and also for magnetic, magneto-electric and MO device applications.

Recently, Feng *et al.* [12] synthesized new double perovskite  $\text{Ba}_2\text{NiOsO}_6$  and found it to be a rare ferromagnetic (FM) semiconductor with Curie temperature  $T_C = 100$  K [12]. It crystallizes in a cubic  $Fm\bar{3}m$  structure with lattice constant  $a = 8.0428 \text{ \AA}$ , where the  $\text{Ni}^{2+}$

and  $\text{Os}^{6+}$  ions are perfectly ordered on the B and B' sites, respectively [12]. This is interesting because FM semiconductors are rare and also useful for the development of spintronic devices. Surprisingly, we note that Ni and Os ions are ferromagnetically coupled, which is very rare between the B and B' cations in double perovskite oxides [13, 14]. Furthermore, first-principles electronic structure calculations [12] showed that the spin-orbit coupling (SOC) of  $\text{Os}^{6+}$  plays a crucial role in opening the semiconducting gap, and thus double perovskite  $\text{Ba}_2\text{NiOsO}_6$  is called a Dirac-Mott insulator. However, it was inferred from the x-ray absorption spectra (XAS) [12] that the formal electronic configurations for Ni and Os in  $\text{Ba}_2\text{NiOsO}_6$  are  $\text{Ni}^{2+} 3d^8 (t_{2g}^6 e_g^2; S = 1; 2 \mu_B)$  and  $\text{Os}^{6+} 5d^2 (t_{2g}^2 e_g^0; S = 1; 2 \mu_B)$ , respectively. Consequently, the total moment should be  $4 \mu_B/\text{f.u.}$  for the FM ground state. However, the measured saturation magnetization for  $\text{Ba}_2\text{NiOsO}_6$  is approximately  $3.46 \mu_B/\text{f.u.}$  at 5 K and 50 kOe, much smaller than the spin only magnetic moment estimated from the simplified ionic model. Therefore, it would be interesting to study the origin of the abnormal ferromagnetism as well as the spin and orbital magnetic moments of  $\text{Ba}_2\text{NiOsO}_6$ .

When a linearly polarized light beam hits a magnetic material, the polarization vector of the reflected and transmitted light beams rotates. The former and latter are known as Kerr and Faraday effects, respec-

\*Electronic address: gyguo@phys.ntu.edu.tw

tively. Discovered in the 19th Century, they are two well-known MO effects [15, 16]. Currently, MO Kerr effect (MOKE) is widely used as a powerful probe of the electronic and magnetic properties of materials, such as two-dimensional ferromagnetic order [17–19], spin Hall effect [20], skyrmion Hall effect [21], magnetic anisotropy [22, 23], and topological insulator [24, 25]. Furthermore, because of its applications in modern high-density data-storage technology [26], an enormous amount of effort has been devoted to search for materials with large MO signals.

Band exchange splitting caused by magnetization together with relativistic SOC has been recognized as the origin of MOKE [15, 16, 27–29]. Localized  $3d$  orbitals tend to have large band exchange splittings. However, their SOC is weak. However,  $4d$  or  $5d$  transition metal atoms have a strong SOC. Nonetheless, their intra-atomic exchange interaction is rather small because of their more extended  $d$  orbitals which result in small band exchange splittings. Therefore, an effective way to enhance the MOKE is to make alloys or multilayers of  $3d$  transition metals with  $4d$  or  $5d$  transition metals [30]. Consequently, the magneto-optical properties of various  $3d$  FM transition metal alloys and multilayers with heavier  $4d$  or  $5d$  transition metal atoms have been investigated extensively. For example, PtMnSb [31] has been found to be an excellent MO metal with a maximum Kerr rotation of  $2.5^\circ$ . Double perovskites,  $A_2BB'O_6$  ( $B = 3d$  and  $B' = 4d$  or  $5d$  transition metal elements), which can establish an unusual renormalization of the intra-atomic exchange strength to enhance the band exchange splitting at the  $4d$  or  $5d$  sites arising from the so called hybridization driven mechanism [32, 33], is also expected to have large MOKE. However, the B and B' atoms in most of double perovskite materials [4, 13, 14] prefer an antiferromagnetic coupling. This may reduce the net magnetization and thus results in a small MO effect [7]. As mentioned above, simultaneous occurrence of ferromagnetism and semiconducting gap in double perovskites is very rare. Combination of the strong SOC of Os atoms and ferromagnetism thus would make  $Ba_2NiOsO_6$  an excellent semiconductor for not only semiconductor-based spintronics but also magneto-optical devices.

The recent development in synthesizing artificial atomic-scale transition metal oxide heterostructures provides great tunability over fundamental physical parameters to realize novel properties and functionalities [34, 35], such as the conductive interface between two insulating oxides [36–38]. This also stimulates extensive investigations on the topology of the electronic band structure of transition metal oxide heterostructures [8, 10, 11, 39–41]. Indeed, the quantum anomalous Hall phase was predicted to occur in (001) double-perovskite  $La_2MnIrO_6$  monolayer [10] and also (111) double-perovskite  $La_2FeMoO_6$  and  $Ba_2FeReO_6$  monolayers [8, 42]. Therefore, it would also be interesting to study the topological properties of Dirac-Mott semiconductor  $Ba_2NiOsO_6$  and its heterostructures.

In this paper, we present a systematic first-principles study of magnetism, electronic structure, magneto-optical effects and topological property of cubic double perovskite  $Ba_2NiOsO_6$  and its (111)  $(Ba_2NiOsO_6)_1/(BaTiO_3)_{10}$  monolayer superlattice. First, we find that both structures are narrow band gap FM semiconductors. The ferromagnetism is driven by the rare nearest-neighbor FM coupling between Ni and Os atoms, which is attributed to the FM superexchange mechanism caused by the abnormally strong hybridization between the half-filled Ni  $e_g$  and unoccupied Os  $e_g$  orbitals. Second, the strong SOC on the Os atom is found to not only open the semiconducting gap but also give rise to a large negative orbital magnetic moment on the Os atom, thus resulting in a measured total magnetic moment of less than  $4 \mu_B/f.u.$  [12]. Third, we also find that because of the enhanced intra-atomic exchange interaction on the Os atoms caused by the Ni  $3d$  - Os  $5d$  hybridization and the strong SOC on the Os site, the MO effects are large in these two structures. Our theoretical findings thus suggest that double perovskite  $Ba_2NiOsO_6$  and its (111) superlattice are valuable ferromagnetic semiconductors for not only semiconductor-based spintronics but also magneto-optical devices. Finally, our calculated anomalous Hall conductivity reveals that the band gap just below the Fermi level in the superlattice is topologically nontrivial with the gap Chern number of 2. This indicates that the (111)  $Ba_2NiOsO_6$  monolayer superlattice and related  $5d$  double-perovskite monolayers may provide an interesting material platform for exploring magnetic topological phases and phase transitions.

## II. THEORY AND COMPUTATIONAL DETAILS

We consider cubic double perovskite  $Ba_2NiOsO_6$  [Fig. 1(a)] and its  $(Ba_2NiOsO_6)_1/(BaTiO_3)_{10}$  monolayer superlattice grown along the [111] direction [Figs. 1(b) and 1(c)]. The Brillouin Zone (BZs) of bulk  $Ba_2NiOsO_6$  and the (111)  $(Ba_2NiOsO_6)_1/(BaTiO_3)_{10}$  superlattice are shown in Figs. 1(e) and 1(f), respectively. Clearly, the latter is the folded BZ of the former along the  $\Gamma$  - L direction. In the present calculations of the electronic structure and magneto-optical properties of bulk  $Ba_2NiOsO_6$ , the experimental lattice constant of  $8.0428 \text{ \AA}$  is adopted. Since the  $BaTiO_3$  slab in the  $(Ba_2NiOsO_6)_1/(BaTiO_3)_{10}$  superlattice is much thicker than the  $Ba_2NiOsO_6$  layer, the  $BaTiO_3$  slab could be regarded as the substrate. Therefore, the in-plane lattice constant is fixed at  $\sqrt{2}a_0 = 5.6962 \text{ \AA}$ , where  $a_0$  is the theoretically determined lattice constant of cubic perovskite  $BaTiO_3$ . In our structural optimization, the in-plane hexagonal symmetry is fixed but lattice constant  $c$  and internal coordinates of all the atoms in the superlattice are optimized theoretically. The lattice parameters and atom positions for bulk  $Ba_2NiOsO_6$  and its (111) monolayer superlattice are given, respectively, in Tables S1 and S2 in the Supple-

mentary Materials (SM) [43]. The electronic structure and magnetic structure are calculated based on the density functional theory (DFT) with the generalized gradient approximation (GGA) [44]. The accurate projector-augmented wave (PAW) method [45], as implemented in the Vienna *ab initio* simulation package (VASP) [46], is used. The relativistic PAW potentials are adopted to include the SOC. The valence configurations of Ba, Ni, Os, Ti and O atoms adopted in the present calculations are  $5s^25p^66s^2$ ,  $3p^63d^84s^2$ ,  $5p^65d^66s^2$ ,  $3s^23p^63d^24s^2$  and  $2s^22p^4$ , respectively. To better account for the on-site electron correlation on the  $d$  shells of Os and Ni atoms, the GGA + U method [47] is adopted with the effective Coulomb repulsion energy  $U_{Os} = 2.0$  eV and  $U_{Ni} = 5.0$  eV, respectively. The results of test calculations using different  $U$  values of  $3 \sim 5$  eV for Ni and  $1 \sim 3$  eV for Os, are given in Appendix A below. A large plane-wave cutoff of 450 eV and the small total energy convergence criterion of  $10^{-5}$  eV are used throughout. Fine Monkhorst-Pack  $k$ -meshes of  $30 \times 30 \times 30$  and  $10 \times 10 \times 2$  are used for the bulk and superlattice calculations, respectively.

To find the ground state magnetic configuration and to understand the magnetic interactions in both systems, we consider four possible magnetic structures, as labeled FM, AFM, FI1, and FI2 in Figs. 2 and 3. One can then evaluate the nearest-neighbor Ni-Os ( $J_1$ ), Os-Os ( $J_2$ ) and Ni-Ni ( $J_3$ ) magnetic coupling parameters by mapping the calculated total energies of the FM, AFM, FI1, and FI2 magnetic configurations to the classical Heisenberg model  $H = E_0 - \sum_{i>j} J_{ij}(\hat{e}_i \cdot \hat{e}_j)$ , where  $J_{ij}$  is the exchange coupling parameter between sites  $i$  and  $j$ , and  $\hat{e}_i$  denotes the direction of spin on site  $i$ .

For a ferromagnetic solid with at least threefold rotational symmetry (i.e., tetragonal, trigonal, hexagonal and cubic) and the magnetization along the rotational  $z$ -axis, the optical conductivity tensor can be written as[48]

$$\sigma = \begin{pmatrix} \sigma_{xx} & \sigma_{xy} & 0 \\ -\sigma_{xy} & \sigma_{yy} & 0 \\ 0 & 0 & \sigma_{zz} \end{pmatrix}. \quad (1)$$

Within linear response Kubo formalism [49], the absorptive parts of the conductivity tensor elements due to interband transitions are given by

$$\sigma_{1aa}(\omega) = \frac{\alpha}{\omega} \sum_{i,j} \int_{BZ} \frac{d\mathbf{k}}{(2\pi)^3} |p_{ij}^a|^2 \delta(\epsilon_{\mathbf{k}j} - \epsilon_{\mathbf{k}i} - \hbar\omega), \quad (2)$$

$$\sigma_{2xy}(\omega) = \frac{\alpha}{\omega} \sum_{i,j} \int_{BZ} \frac{d\mathbf{k}}{(2\pi)^3} \text{Im}[p_{ij}^x p_{ji}^y] \delta(\epsilon_{\mathbf{k}j} - \epsilon_{\mathbf{k}i} - \hbar\omega), \quad (3)$$

where summations  $i$  and  $j$  are over the valence and conduction bands, respectively.  $\alpha = \frac{\pi e^2}{\hbar m^2}$  is a material specific constant,  $\hbar\omega$  is the photon energy, and  $\epsilon_{\mathbf{k}i}$  is the  $i$ th band energy at  $\mathbf{k}$  point. Dipole matrix elements  $p_{ij}^a = \langle \mathbf{k}j | \hat{p}_a | \mathbf{k}i \rangle$  where  $\hat{p}_a$  denotes Cartesian component  $a$

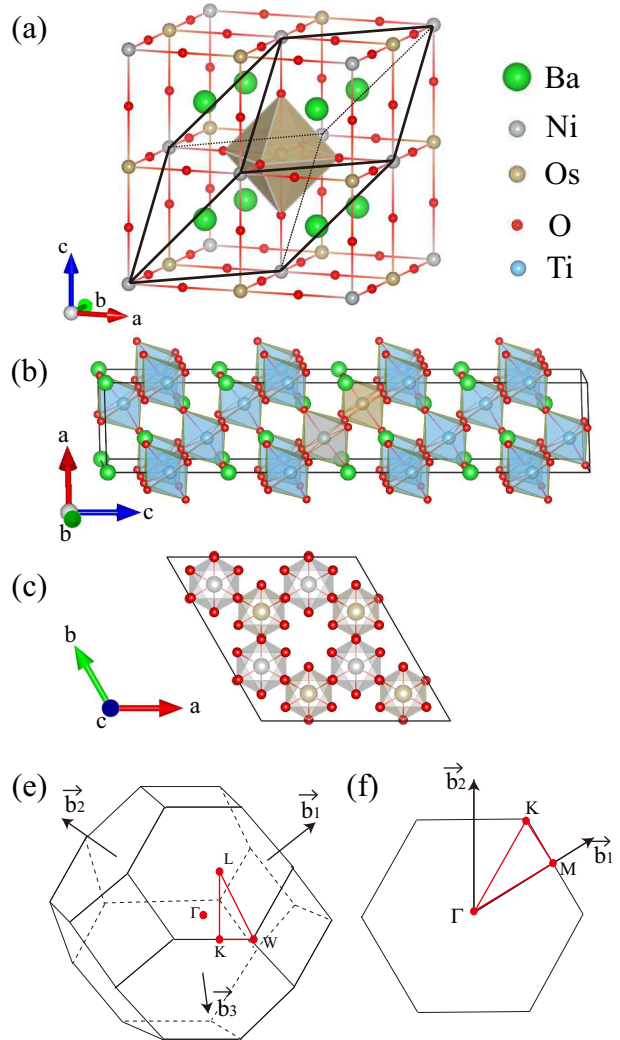


FIG. 1: (a) Cubic crystal cell of bulk  $\text{Ba}_2\text{NiOsO}_6$ . Black lines indicate the fcc primitive unit cell. (b) Side view and (c) top view of the crystal structure of the (111)  $(\text{Ba}_2\text{NiOsO}_6)_1/(\text{Ba}_2\text{TiO}_3)_{10}$  superlattice. In (c), two different colors denote the X atoms on the two different planes in the (111)  $\text{Ba}_2\text{NiOsO}_6$  monolayer forming a buckled honeycomb lattice. (e) The Brillouin Zone of bulk  $\text{Ba}_2\text{NiOsO}_6$  and (f) the BZ of its (111)  $(\text{Ba}_2\text{NiOsO}_6)_1/(\text{Ba}_2\text{TiO}_3)_{10}$  superlattice, with the basis vectors  $\vec{b}_1$ ,  $\vec{b}_2$  and  $\vec{b}_3$  of the reciprocal lattices as well as some high-symmetry points labeled.

of the dipole operator, are obtained from the band structures within the PAW formalism[50], as implemented in the VASP package. The integration over the BZ is carried out by using the linear tetrahedron method (see Ref. [51] and references therein). The dispersive parts of the conductivity tensor elements can be obtained from the corresponding absorptive parts by use of the Kramer-Kronig transformation [52],

$$\sigma_{2aa}(\omega) = -\frac{2\omega}{\pi} P \int_0^\infty \frac{\sigma_{1aa}(\omega')}{\omega'^2 - \omega^2} d\omega', \quad (4)$$

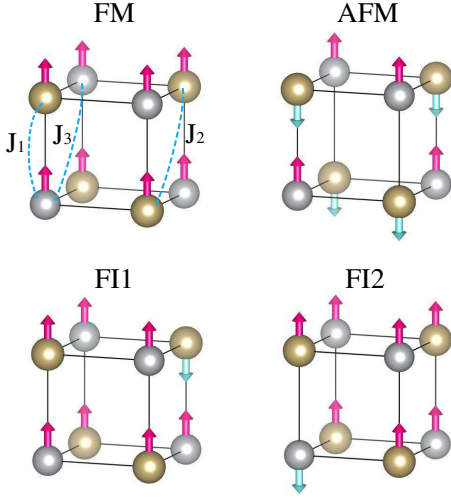


FIG. 2: (a) Ferromagnetic (FM), (b) antiferromagnetic (AFM), (c) type I ferrimagnetic (FI1) and (d) type II ferrimagnetic (FI2) configurations in bulk  $\text{Ba}_2\text{NiOsO}_6$ .

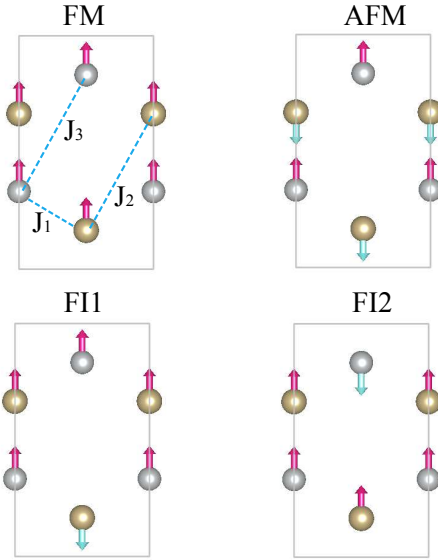


FIG. 3: (a) Ferromagnetic (FM), (b) antiferromagnetic (AFM), (c) type I ferrimagnetic (FI1) and (d) type II ferrimagnetic (FI2) configurations in (111) monolayer  $\text{Ba}_2\text{NiOsO}_6$ .

$$\sigma_{1xy}(\omega) = \frac{2}{\pi} P \int_0^\infty \frac{\omega' \sigma_{2xy}(\omega')}{\omega'^2 - \omega^2} d\omega', \quad (5)$$

where  $P$  denotes the principal integral.

In the polar geometry, the complex Kerr angle can then be calculated from the optical conductivity tensor via [53, 54],

$$\theta_K + i\varepsilon_K = \frac{-\sigma_{xy}}{\sigma_{xx} \sqrt{1 + i(4\pi/\omega)\sigma_{xx}}}, \quad (6)$$

which  $\theta_K$  is the Kerr rotation angle and  $\varepsilon_K$  the Kerr ellipticity. For a magnetic thin film, the complex Faraday

rotation angle can be written as [? ],

$$\theta_F + i\varepsilon_F = \frac{\omega d}{2c} (n_+ - n_-), \quad (7)$$

where  $n_+$  and  $n_-$  represent the refractive indices for left- and right-handed polarized lights, respectively, and are related to the corresponding dielectric function (or optical conductivity via expressions  $n_\pm^2 = \varepsilon_\pm = 1 + \frac{4\pi i}{\omega} \sigma_\pm = 1 + \frac{4\pi i}{\omega} (\sigma_{xx} \pm i\sigma_{xy})$ ). For many magnetic materials, the  $\sigma_{xx}$  is generally much larger than the corresponding  $\sigma_{xy}$ . Therefore,  $n_\pm = [1 + \frac{4\pi i}{\omega} (\sigma_{xx} \pm i\sigma_{xy})]^{1/2} \approx [1 + \frac{4\pi i}{\omega} \sigma_{xx}]^{1/2} \mp \frac{2\pi}{\omega} (\sigma_{xy} / \sqrt{1 + \frac{4\pi i}{\omega} \sigma_{xx}})$ . Consequently,

$$\theta_F + i\varepsilon_F \approx -\frac{2\pi d}{c} \frac{\sigma_{xy}}{\sqrt{1 + \frac{4\pi i}{\omega} \sigma_{xx}}}. \quad (8)$$

The anomalous Hall conductivity (AHC) is calculated based on the Berry-phase formalism [56]. Within this Berry-phase formalism, the AHC ( $\sigma_{ij}^A = J_i^c / E_j$ ) is given as a BZ integration of the Berry curvature for all the occupied (valence) bands,

$$\sigma_{xy}^A = -\frac{e^2}{\hbar} \sum_{n \in VB} \int_{BZ} \frac{d\mathbf{k}}{(2\pi)^3} \Omega_{xy}^n(\mathbf{k}), \quad (9)$$

$$\Omega_{xy}^n(\mathbf{k}) = -\sum_{n' \neq n} \frac{2\text{Im}[p_{ij}^x p_{ji}^y]}{(\epsilon_{\mathbf{k}n} - \epsilon_{\mathbf{k}n'})^2},$$

where  $\Omega_{ij}^n(\mathbf{k})$  is the Berry curvature for the  $n$ th band at  $\mathbf{k}$ .  $J_i^c$  is the  $i$  component of the charge current density  $\mathbf{J}^c$  and  $E_j$  is the  $j$ -component of the electric field  $\mathbf{E}$ . Note that the AHC is nothing but  $\sigma_{1xy}(\omega)$  in the dc limit, i.e.,  $\sigma_{xy}^A = \sigma_{1xy}(\omega = 0)$ . From the Kramers-Kronig relations, we can obtain a sum rule for  $\sigma_{1xy}(\omega = 0)$ ,

$$\sigma_{1xy}(\omega = 0) = \frac{2}{\pi} P \int_0^\infty \frac{\sigma_{2xy}(\omega')}{\omega'} d\omega'. \quad (10)$$

Putting Eq.(3) into this sum rule would result in Eq. (9). Since a large number of  $k$  points are needed to get accurate AHCs, we use the efficient Wannier interpolation method [57, 58] based on maximally localized Wannier functions (MLWFs) [59]. Since the energy bands around the Fermi level are dominated by Os  $t_{2g}$  orbitals, 6 MLWFs per unit cell of Os  $t_{2g}$  orbitals are constructed by fitting to the GGA+U+SOC band structure in the energy window from -0.69 eV to 2.51 eV for the bulk, and from -0.54 eV to 1.66 eV for the monolayer. The band structure obtained by the Wannier interpolation agrees well with that from the GGA+U+SOC calculation. The AHC ( $\sigma_{xy}^A$ ) was then evaluated by taking a very dense k-point mesh of  $200 \times 200 \times 200$  and  $200 \times 200 \times 1$  in the BZ for bulk  $\text{Ba}_2\text{NiOsO}_6$  and its (111) monolayer, respectively.

TABLE I: The properties of bulk and (111) monolayer  $\text{Ba}_2\text{NiOsO}_6$  from the GGA+U calculations.  $E_{FM}$ ,  $E_{AFM}$ ,  $E_{FI1}$ , and  $E_{FI2}$  denote the total energies of the FM, AFM, FI1, and FI2 configurations, respectively (see Figs. 2 and 3).  $J_1$  ( $d_{\text{Ni-Os}}$ ),  $J_2$  ( $d_{\text{Os-Os}}$ ), and  $J_3$  ( $d_{\text{Ni-Ni}}$ ) represent the nearest Ni-Os, Os-Os, and Ni-Ni exchange coupling parameters (interatomic distances), respectively.  $T_c$  is the magnetic ordering temperature.

	Bulk	(111) monolayer
$E_{FM}$ (meV/f.u.)	0	0
$E_{AFM}$ (meV/f.u.)	77.80	35.57
$E_{FI1}$ (meV/f.u.)	61.89	6.635
$E_{FI2}$ (meV/f.u.)	38.20	17.57
$d_{\text{Ni-Os}}$ (Å)	4.021	4.103
$d_{\text{Os-Os}}$ (Å)	5.687	5.696
$d_{\text{Ni-Ni}}$ (Å)	5.687	5.696
$J_1$ (meV)	6.48	5.928
$J_2$ (meV)	2.87	-2.787
$J_3$ (meV)	-0.09	-0.054
$T_c$ (K)	$\sim 150$ ( $\sim 100^a$ )	$\sim 69$

<sup>a</sup>Experimental value from Ref. [12].

### III. RESULTS AND DISCUSSION

#### A. Magnetic properties

We study four magnetic configurations in both bulk  $\text{Ba}_2\text{NiOsO}_6$  and its (111) monolayer, as illustrated in Figs. 2 and 3, respectively. The calculated total energies of these magnetic configurations are listed in Table I. It is clear that in both structures the FM configuration is the ground state. Therefore, we list in Table II the calculated magnetic moments and band gap of only the FM state. Table II shows that in bulk  $\text{Ba}_2\text{NiOsO}_6$ , both Ni and Os atoms have large spin magnetic moments, being  $1.78 \mu_B$  and  $1.22 \mu_B$ , respectively. Nevertheless, because of the hybridization among O  $p$ , Os  $d$ , and Ni  $d$  orbitals, these spin magnetic moments fall short of  $2.0 \mu_B$  expected from  $\text{Ni}^{2+} 3d^8 (t_{2g}^6 e_g^2; S = 1)$  and  $\text{Os}^{6+} 5d^2 (t_{2g}^2 e_g^0; S = 1)$  ions. Interestingly, both Ni and especially Os atoms have significant orbital magnetic moments, being  $0.21 \mu_B$  and  $-0.55 \mu_B$ , respectively. Hund's second rule states that the spin and orbital moments would be antiparallel if the  $d$  shell is less than half-filled, and otherwise they would be parallel. In consistence with Hund's second rule, the Ni orbital moment is parallel to the Ni spin moment while the Os orbital moment is antiparallel to the Os spin moment. Consequently, because of the large negative Os orbital moment, the total magnetic moment is  $3.37 \mu_B/\text{f.u.}$  in bulk  $\text{Ba}_2\text{NiOsO}_6$ . This theoretical value agrees rather well with the total magnetic moment of  $3.46 \mu_B/\text{f.u.}$  deduced from the magnetic susceptibility experiment [12]. The calculated magnetic moments for the (111)  $\text{Ba}_2\text{NiOsO}_6$  monolayer are similar to that of bulk  $\text{Ba}_2\text{NiOsO}_6$  (see Table II).

As mentioned before, using the calculated total energies for the four magnetic configurations, we evaluate the exchange coupling parameters between magnetic atoms.

TABLE II: Spin ( $m_s$ ) and orbital ( $m_o$ ) magnetic moments as well as band gap ( $E_g$ ) of ferromagnetic  $\text{Ba}_2\text{NiOsO}_6$  and its (111) monolayer from the GGA+U+SOC calculations. The magnetization is along the  $c$ -axis.

	Bulk	(111) monolayer
$m_s^{Os}$ ( $\mu_B/\text{atom}$ )	1.22	1.22
$m_o^{Os}$ ( $\mu_B/\text{atom}$ )	-0.55	-0.50
$m_s^{Ni}$ ( $\mu_B/\text{atom}$ )	1.78	1.75
$m_o^{Ni}$ ( $\mu_B/\text{atom}$ )	0.21	0.21
$m_s^O$ ( $\mu_B/\text{f.u.}$ )	0.61	0.61
$m_o^O$ ( $\mu_B/\text{f.u.}$ )	-0.08	-0.14
$m_t^{Os}$ ( $\mu_B/\text{atom}$ )	0.67 (0.97 <sup>a</sup> )	0.72
$m_t^{Ni}$ ( $\mu_B/\text{atom}$ )	1.99 (2.13 <sup>a</sup> )	1.96
$m_t^{tot}$ ( $\mu_B/\text{f.u.}$ )	3.37 (3.46 <sup>a</sup> )	3.78
$E_g$ (eV)	0.22 (0.31 <sup>a</sup> )	0.37

<sup>a</sup>Experimental values from Ref. [12].

The obtained nearest neighbor Ni-Os ( $J_1$ ), Os-Os ( $J_2$ ), and Ni-Ni ( $J_3$ ) exchange coupling parameters together with their distances are listed in Table I. Interestingly, in both systems the magnetic interaction between B (Ni) and B' (Os) is ferromagnetic and is rather strong. This FM coupling between B and B' cations is very rare in double perovskite oxides [4, 14]. This explains why the FM state is the ground state, quite unlike many other double perovskite oxides in which the AFM is often favored [4, 14]. The second near neighbor Os-Os exchange coupling ( $J_2$ ) is, however, AFM in the monolayer, although it is still FM in the bulk (Table I). Furthermore, the second near neighbor Ni-Ni magnetic coupling ( $J_3$ ) is much smaller than  $J_1$ . The smallness of  $J_3$  could be attributed to the much localized Ni  $3d$  orbitals in comparison with that of Os  $5d$  orbitals. Note that we also perform the total energy calculations for the (111)  $\text{Ba}_2\text{NiOsO}_6$  monolayer superlattice in the zigzag-AFM and stripy-AFM configurations (see Figs. 2(c) and 2(d) in Ref. [41]) to estimate the next-nearest neighbor Ni-Os coupling parameter ( $J_{\text{Ni-Os}}^{\text{NN}}$ ). We obtain a small  $J_{\text{Ni-Os}}^{\text{NN}}$  value of 0.12 meV. This is much smaller than the nearest neighbor Ni-Os exchange coupling parameter (see  $J_1$  in Table I), and thus the  $J_{\text{Ni-Os}}^{\text{NN}}$  values are not listed in Table I.

Based on the calculated  $J_1$  values, we could estimate magnetic ordering temperature ( $T_c$ ) within a mean-field approximation given by  $k_B T_c = \frac{1}{3} z J_1$  where  $z$  is the number of Ni-Os pairs for either Ni or Os atom. Table I shows that such estimated  $T_c$  of 150 K for the bulk agrees quite well with the experimental value of 100 K [12]. The estimated  $T_c$  of 69 K for the monolayer is smaller than that of the bulk. This could be expected because of the number of nearest Ni-Os exchange couplings decreases from six in the bulk to three in the monolayer.

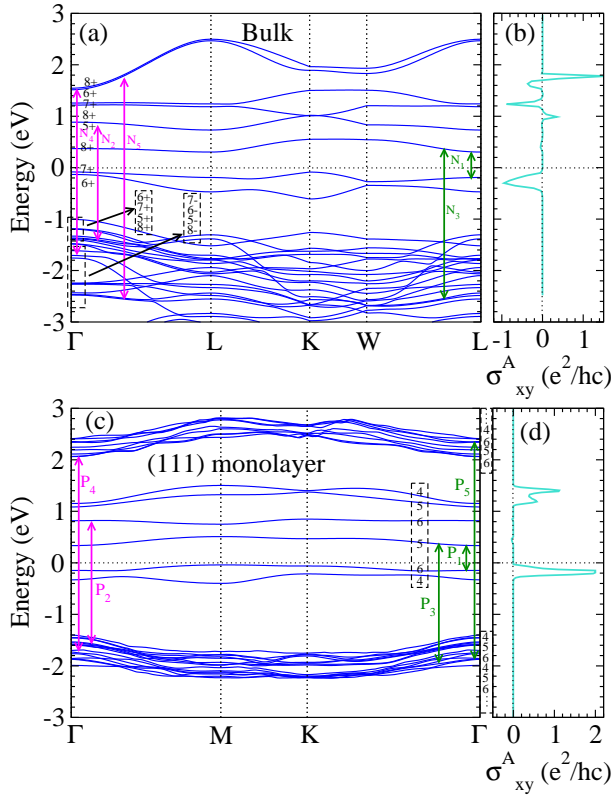


FIG. 4: (a, c) Relativistic band structure and (b, d) anomalous Hall conductivity ( $\sigma_{xy}^A$ ) of bulk  $\text{Ba}_2\text{NiOsO}_6$  (upper panels) and its (111) monolayer (lower panels). The FM magnetization is along the  $c$  axis. The zero of energy is placed at the top of valence bands. In (c), only the  $\text{Ba}_2\text{NiOsO}_6$  monolayer-dominated bands are displayed (see the maintext). The symmetry of band states at the  $\Gamma$  point are labeled according to the irreducible representations listed in Tables IV and V in Appendix C. The principal inter-band transitions and the corresponding peaks in the  $\sigma_{xy}$  in Figs. 8(c) and 9(c) are indicated by pink and green arrows.

## B. Electronic structure

Now let us examine the FM electronic structure of bulk  $\text{Ba}_2\text{NiOsO}_6$  and its (111) ( $\text{Ba}_2\text{NiOsO}_6$ )<sub>1</sub>( $\text{BaTiO}_3$ )<sub>10</sub> monolayer superlattice, which is needed for the following discussion of the optical conductivity tensor and the magneto-optical effects. The calculated fully relativistic and scalar-relativistic band structures are plotted in Figs. 4 and 5, respectively. For clarity and ease of comparison with bulk, we only show the main contributions from monolayer  $\text{Ba}_2\text{NiOsO}_6$  for (111) superlattice. Furthermore, the calculated atom- and orbital-decomposed densities of states (DOSs) for both structures are displayed in Fig. 6. Figure 4 shows that both structures are a semiconductor with a small indirect band gap (Table II). Figure 6 indicates that the band gap falls within the spin-up Os  $5d$   $t_{2g}$  dominant bands. In bulk  $\text{Ba}_2\text{NiOsO}_6$ , the calculated band gap of 0.22 eV is comparable to the experimental one of  $\sim 0.31$  eV [12]. Interestingly,

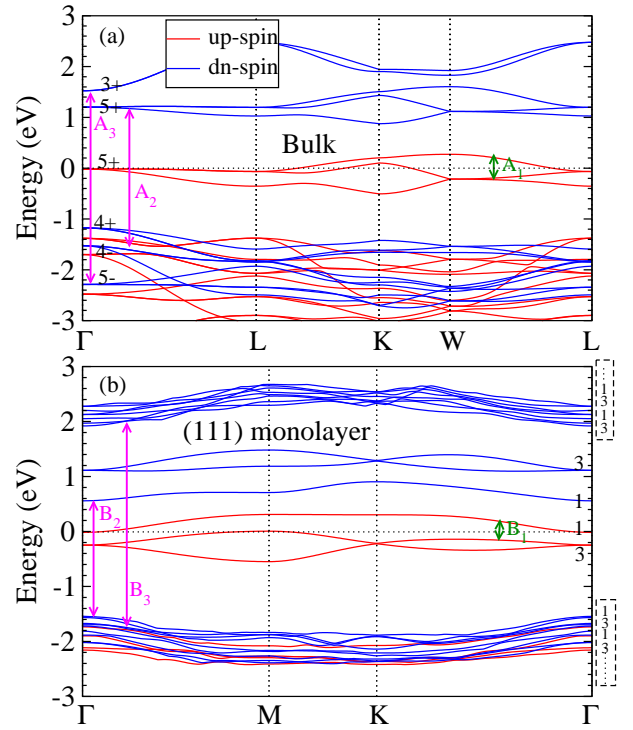


FIG. 5: Scalar-relativistic band structures of bulk  $\text{Ba}_2\text{NiOsO}_6$  (a) and its (111) monolayer (b). The zero of energy is placed at the top of valence bands. In panel (b), only the  $\text{Ba}_2\text{NiOsO}_6$  monolayer dominated bands are displayed (see the maintext). The symmetry of band states at the  $\Gamma$  point are labeled according to the irreducible representations listed in Tables IV and V in Appendix C. The principal inter-band transitions and the corresponding peaks in the  $\sigma_{1xx(zz)}$  in Figs. 7(a) and 7(c) are indicated by pink arrows.

the scalar-relativistic band structures of bulk  $\text{Ba}_2\text{NiOsO}_6$  and its (111) monolayer are a metal and a semi-metal (Fig. 5), respectively. When the SOC is included, the  $t_{2g}$  (equivalent to  $l = 1$ ) states split into doubly degenerate ( $j = 3/2$ ) occupied state and nondegenerate ( $j = 1/2$ ) unoccupied state (Fig. 6). This confirms that the SOC plays an essential role in the semiconducting gap-opening, and thus  $\text{Ba}_2\text{NiOsO}_6$  is known as a very rare FM Dirac-Mott insulator [12].

Generally speaking, the DOS of the bulk and the (111) monolayer are rather similar (see Fig. 6). The energy bands near Fermi level are predominantly of the Os  $5d$  orbitals. The Os  $5d$  and Ni  $3d$  bands appear in the energy regions of  $-7.8 \sim -3.6$  eV and  $-0.8 \sim 2.4$  eV with significant inter-orbital mixing as well as some small admixture of O  $2p$  states, while the O  $2p$  bands are mainly located between them. Consequently, because of the strong Ni  $3d$  - Os  $5d$  hybridization through the O  $2p$  orbital, the Os  $5d$  states are split into bonding and anti-bonding states. The bonding bands occur in the energy range from  $-6.8$  eV to  $-4.8$  eV, while the anti-bonding ones are located in the region from  $-0.8$  to  $1.6$  eV in the vicinity of the Fermi level. However, compared with the bulk band structure,

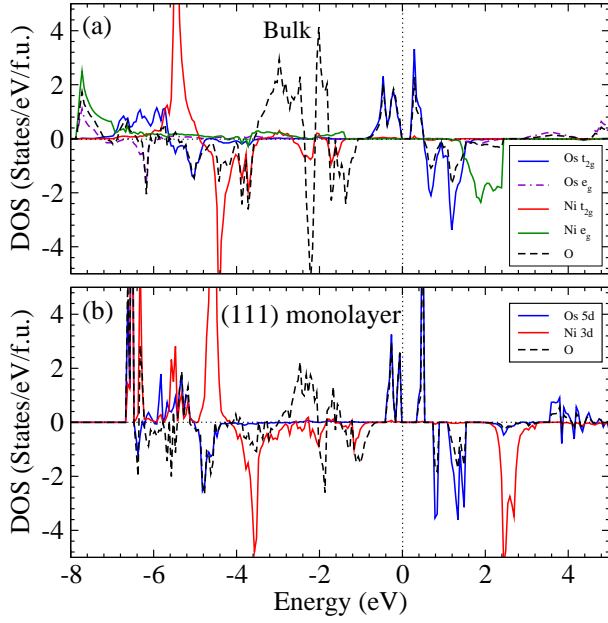


FIG. 6: Os 5d, O, and Ni 3d partial densities of states (DOS) of bulk  $\text{Ba}_2\text{NiOsO}_6$  (a) and its (111) monolayer (b). The zero of energy is placed at the top of valence bands.

although the bandwidths of the 6 Os 5d  $t_{2g}$ -dominated bands near the Fermi level in the monolayer are only slightly reduced, the bandwidths of the lower valence bands and upper conduction bands further away from the Fermi level become noticeably narrowed (see Figs. 4 and 5), due to the reduced number of neighboring Os atoms in the monolayer. Significantly, there are bands crossings at K points, forming the so-called Dirac nodal points in (111) monolayer; In contrast, these band crossings do not occur at the corresponding W point in bulk  $\text{Ba}_2\text{NiOsO}_6$  (Fig. 5). This difference would result in contrasting topological properties of the two systems, as will be discussed in Sec. III E below.

In the cubic double perovskite structure, the crystal field at the transition metal atoms, which sit at the centers of the oxygen octahedrons and occupy the perovskite B sites alternatively, should split the  $d$  states into two upper energy levels  $e_g(3z^2 - 1, x^2 - y^2)$  and three bottom energy levels  $t_{2g}(xy, yz, \text{ and } xz)$ . However, the electronic structure of Ni 3d in the cubic  $\text{Ba}_2\text{NiOsO}_6$  do not follow the theory of crystal field. In Fig. 5(a), it is clearly that Ni  $e_g$  states lies lower than Ni  $t_{2g}$  states in the up-spin channel. Additionally, the exchange splitting energy between the up-spin and down-spin 3d  $e_g$  electrons on the Ni atom is about 9.7 eV, much larger than that of Ni 3d  $t_{2g}$  bands of  $\sim 1.0$  eV. This is because that  $e_g$  orbitals with the wave function directly pointing to that of O  $2p$  orbitals have much stronger hybridization with O  $2p$  states than that of  $t_{2g}$  bands, which causes the bonding occupied  $e_g$  states shift to the lower energy level and the anti-bonding unoccupied  $e_g$  ones move toward the higher energy direction. Moreover, it is interesting to find that

the exchange splitting of Os 5d (up to  $\sim 1.2$  eV) states is large, being comparable to the Ni 3d band exchange splitting, which is due to the unusual renormalization of the intra-atomic exchange strength at the Os sites arising from the Os-Ni interaction, similar to the case of  $\text{Sr}_2\text{FeMoO}_6$  [32].

Two different mechanisms of magnetism in double perovskite oxides have been proposed in the earlier literatures. One is the hybridization-driven mechanism [33] which leads to a negative spin polarization at the 4d or 5d site, that is, the intrinsic spin splitting at the 3d site and an induced spin splitting at the 4d or 5d site which is oppositely aligned. However, in  $\text{Ba}_2\text{NiOsO}_6$ , the Os 5d and Ni 3d states is ferromagnetic rather than anti-ferromagnetic coupling. Thus, the hybridization-driven mechanism is not the origin of the magnetic coupling between Ni 3d ions and Os 5d ions in  $\text{Ba}_2\text{NiOsO}_6$ . The other is the well-known superexchange mechanism based on Goodenough-Kanamori (G-K) rules [60]. In  $\text{Ba}_2\text{NiOsO}_6$ , Ni  $t_{2g}$  orbitals are completely filled, and this rules out Os  $t_{2g}$ - Ni  $t_{2g}$  interaction. Although Ni  $e_g$  orbitals are half-filled and Os  $t_{2g}$  orbitals are partially filled, they are orthogonal and thus do not contribute to the magnetic exchange. The remaining superexchange interaction is between half-filled Ni  $e_g$  and empty Os  $e_g$  orbitals, which should lead to the ferromagnetic coupling. Generally speaking, being a 5d transition metal, Os has a large  $t_{2g}$ - $e_g$  crystal-field splitting, thus driving the  $e_g$  states out of the FM coupling picture in such systems as  $\text{Sr}_2\text{NiOsO}_6$  and  $\text{Ca}_2\text{NiOsO}_6$ . Nevertheless, Ni  $e_g$  and Os  $e_g$  orbitals could hybridize strongly, as shown clearly in Fig. 6. It is this interaction between the Ni  $e_g$  and Os  $e_g$  orbitals that leads to the strong ferromagnetic coupling between the Ni and Os ions in  $\text{Ba}_2\text{NiOsO}_6$ .

### C. Optical conductivity

We calculate the optical conductivity tensors of bulk  $\text{Ba}_2\text{NiOsO}_6$  and its (111) monolayer. The diagonal elements  $\sigma_{xx}$  (for in-plane electric field polarization  $\mathbf{E} \perp \mathbf{c}$ ) and  $\sigma_{zz}$  (for out-of-plane electric field polarization  $\mathbf{E} \parallel \mathbf{c}$ ) of the optical conductivity are displayed in Fig. 7 for both systems. Overall, the calculated spectra of the diagonal elements for the different electric field polarizations in bulk  $\text{Ba}_2\text{NiOsO}_6$  are very similar, i.e., this material is optically isotropic. In particular, they have several identical peaks. Taking the  $\sigma_{1xx}$  and  $\sigma_{1zz}$  spectra as an example, there are a small peak around 0.7 eV, a prominent twin peak centered at 3.0 and 3.5 eV, and a broad valley from 5.6 to 8.4 eV. This optical isotropy could be expected from such highly symmetric crystals as cubic double perovskites. However, for the (111) superlattice, surprisingly,  $\sigma_{1xx}$  and  $\sigma_{1zz}$  are also similar. The reduced symmetry in the superlattice causes only small differences. For example, the prominent  $B_3$  peak at  $\sim 4.2$  eV in the  $\sigma_{1xx}$  spectrum is only slightly higher than that in the  $\sigma_{1zz}$  spectrum [see Fig. 7(c)] due to the reduced crystal sym-

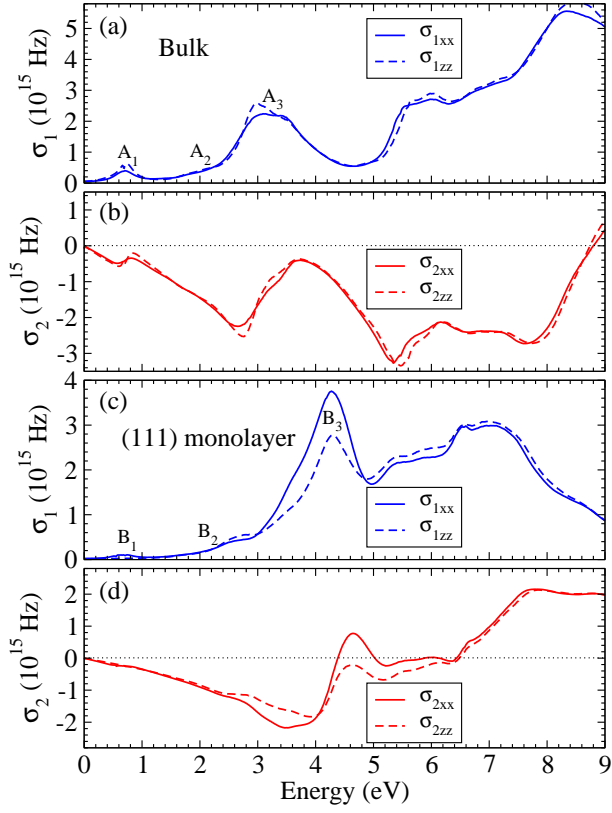


FIG. 7: (a, c) Real part ( $\sigma_1$ ) and (b, d) imaginary part ( $\sigma_2$ ) of the diagonal elements of the optical conductivity tensor of bulk  $\text{Ba}_2\text{NiOsO}_6$  (a, b) and its (111)( $\text{Ba}_2\text{NiOsO}_6$ )<sub>1</sub>/( $\text{BaTiO}_3$ )<sub>10</sub> monolayer superlattice (c, d).

metry. Nevertheless, compared with bulk case, although the spectral lines of (111) superlattice are similar at low frequency region, the peaks in high energy, such as  $B_3$  peak, are noticeably higher and narrower. This can be attributed to the noticeably narrowed bandwidths of the energy bands further away from the Fermi level [see Fig. 5(b)], as mentioned in the preceding subsection.

The real ( $\sigma_{1xy}$ ) and imaginary ( $\sigma_{2xy}$ ) parts of the off-diagonal element of the optical conductivity for bulk  $\text{Ba}_2\text{NiOsO}_6$  are shown in Figs. 8(a) and 8(c), respectively. These spectra exhibit pronounced oscillatory peaks. Notably, a large positive peak appears at  $\sim 3.2$  eV in  $\sigma_{1xy}$ , and that in  $\sigma_{2xy}$  emerges near 2.0 and 3.5 eV. They also have a pronounced negative peak at  $\sim 2.5$  eV in  $\sigma_{1xy}$  and  $\sim 2.9$  eV in  $\sigma_{2xy}$ . Positive (negative)  $\sigma_{2xy}$  suggests that the inter-band transitions are dominated by the excitations due to the left-circularly (right-circularly) polarized light. For example, the negative value in  $\sigma_{2xy}$  around 2.9 eV suggests that inter-band transitions induced by right-circularly polarized light should be stronger. However, the peaks near 2.0 and 3.5 eV indicate the dominance of inter-band transitions due to left-circularly polarized light.

Broadly speaking, the  $\sigma_{1xy}$  and  $\sigma_{2xy}$  for the (111)

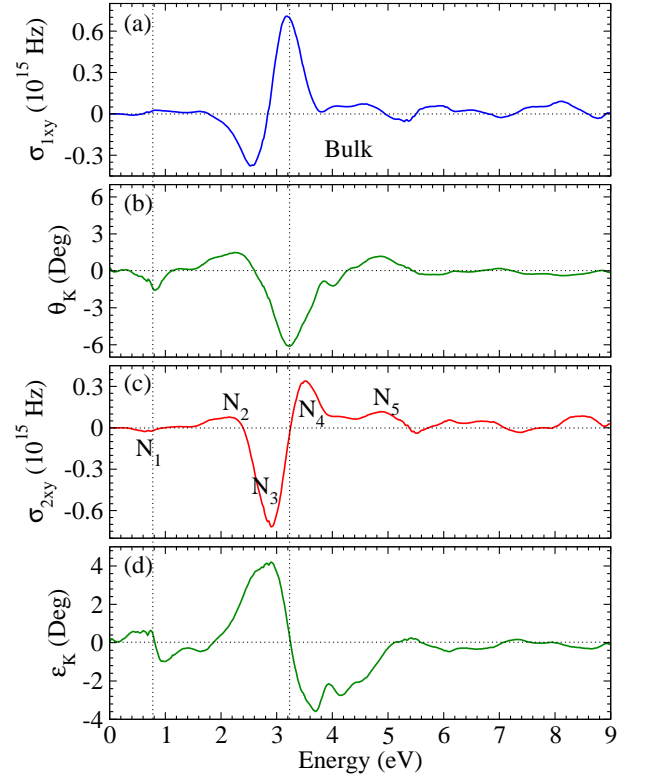


FIG. 8: (a) Real part ( $\sigma_{1xy}$ ) and (c) imaginary part ( $\sigma_{2xy}$ ) of the off-diagonal element of the optical conductivity tensor as well as (b) Kerr rotation angle ( $\theta_K$ ) and (d) Kerr ellipticity ( $\epsilon_K$ ) of bulk  $\text{Ba}_2\text{NiOsO}_6$ .

$\text{Ba}_2\text{NiOsO}_6$  monolayer, shown in Figs. 9(a) and 9(c), respectively, are similar to that of the bulk spectra, and the positive peak positions such as 3.2 eV in  $\sigma_{1xy}$ ,  $\sim 2.0$  and 3.5 eV in  $\sigma_{2xy}$ , remain unchanged. Nevertheless, differences exist for the negative peak positions. For example, negative peaks appear at  $\sim 2.2$  and  $\sim 4.1$  eV in  $\sigma_{1xy}$ , and at  $\sim 2.7$  and  $\sim 4.3$  eV in  $\sigma_{2xy}$ , respectively.

As Eqs. (2) and (3) suggest, the absorptive parts of the optical conductivity elements, i.e.,  $\sigma_{1xx}$  and  $\sigma_{2xy}$ , are directly related to the dipole-allowed inter-band transitions. This would allow us to understand the origins of the main peaks in the  $\sigma_{1xx}$  and  $\sigma_{2xy}$  spectra by determining the symmetries of the calculated band states and the dipole selection rules. The symmetries of band states at the  $\Gamma$ -point of the scalar-relativistic and relativistic band structures of bulk  $\text{Ba}_2\text{NiOsO}_6$  and its (111) monolayer are displayed in Figs. 4 and 5. Using the dipole selection rules (see Tables VI and VII in Appendix C), we could assign the main peaks in the  $\sigma_{1xx}$  in Fig. 7(a) and 7(c) and the  $\sigma_{2xy}$  in Fig. 8(c) and Fig. 9(c) to the inter-band transitions at the  $\Gamma$  point displayed in Figs. 4 and 5 for the two systems. Taking bulk  $\text{Ba}_2\text{NiOsO}_6$  as an example, we could relate the  $A_3$  peak at  $\sim 3$  eV in the  $\sigma_{1xx}$  [see Fig. 7(a)] to the inter-band transition mainly from the  $\Gamma_4^-$  or  $\Gamma_5^-$  state of the down-spin valence band to the conduction band state  $\Gamma_5^+$  or  $\Gamma_3^+$ . Of course, in addition



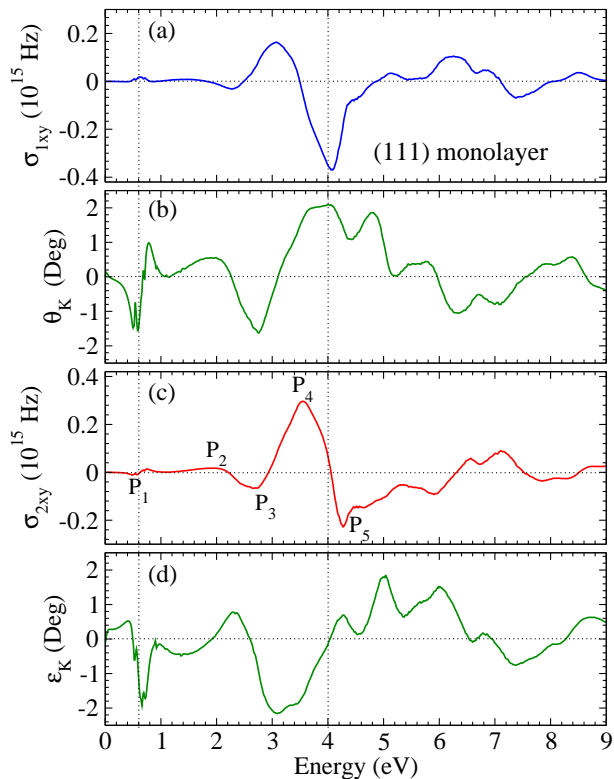


FIG. 9: (a) Real part ( $\sigma_{1xy}$ ) and (c) imaginary part ( $\sigma_{2xy}$ ) of the off-diagonal element of the optical conductivity tensor as well as (b) Kerr rotation angle ( $\theta_K$ ) and (d) Kerr ellipticity ( $\epsilon_K$ ) of the (111)  $(\text{Ba}_2\text{NiOsO}_6)_1/(\text{BaTiO}_3)_{10}$  monolayer superlattice.

to this, there may be contributions from different inter-band transitions at other  $k$  points. Note that without SOC, these band states are doubly degenerate. When the SOC is included, these band states split [see Fig. 4(a)], and this results in the magnetic circular dichroism. Therefore, we could assign the main peaks in the  $\sigma_{2xy}$  to the principal inter-band transitions at the  $\Gamma$ -point only in the relativistic band structure, e.g., displayed in Fig. 4(a). In particular, we could attribute the pronounced peak  $N_3$  at  $\sim 3.0$  eV in the  $\sigma_{2xy}$  in Fig. 8(c) to the inter-band transition from the  $\Gamma_5^-, \Gamma_6^-, \Gamma_7^-$  or  $\Gamma_8^-$  states of valence band to the bottom conduction band state  $\Gamma_5^+$  or  $\Gamma_8^+$  shown in Fig. 4(a).

#### D. Magneto-optical Kerr and Faraday effects

After examining the electronic, magnetic, and optical properties of bulk  $\text{Ba}_2\text{NiOsO}_6$  and its (111) monolayer, let us now turn our attention to their magneto-optical Kerr and Faraday effects. The calculated complex Kerr rotation angles of bulk and (111) monolayer  $\text{Ba}_2\text{NiOsO}_6$  are displayed in Figs. 8 and 9, respectively. For bulk  $\text{Ba}_2\text{NiOsO}_6$ , the Kerr rotation angle is remarkably large, reaching up to  $-1.5^\circ$  at  $\sim 0.8$  eV,  $1.5^\circ$  at  $\sim 2.3$  eV and

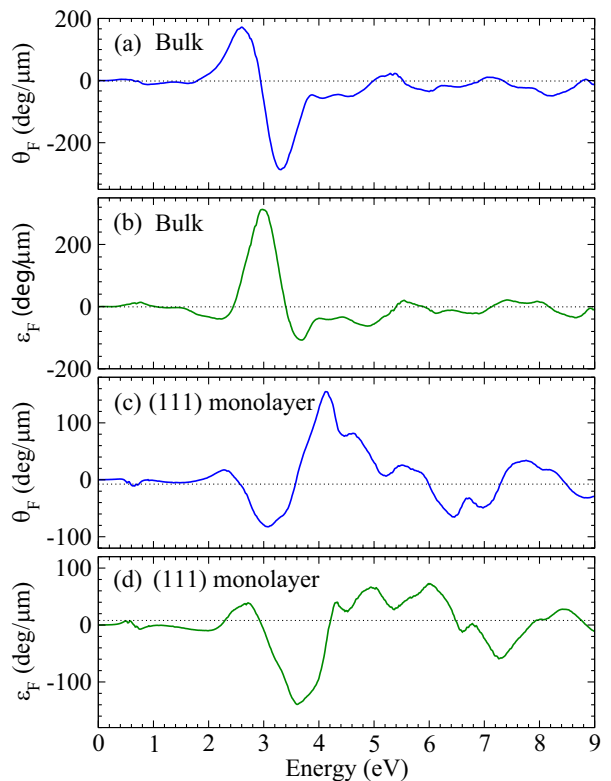


FIG. 10: (a, c) Faraday rotations ( $\theta_F$ ) and (b, d) Faraday ellipticities ( $\epsilon_F$ ) of bulk  $\text{Ba}_2\text{NiOsO}_6$  (upper two panels) and its (111) monolayer (lower two panels).

$-6^\circ$  at  $\sim 3.2$  eV. These large values imply that the large MOKE exists in bulk  $\text{Ba}_2\text{NiOsO}_6$ . As discussed already in Sec. I, this large MOKE stems from the combined effect of the enhanced band exchange splitting of the Os  $5d$   $t_{2g}$  orbitals caused by the significant Ni  $3d$  - Os  $5d$  hybridization and the strong SOC of the Os atoms [30]. The shape of the Kerr rotation spectrum for the (111) superlattice, shown in Fig. 9, is similar to that of bulk  $\text{Ba}_2\text{NiOsO}_6$ . The notable difference between the two systems is the amplitude of the prominent peaks. The Kerr rotation angles get reduced in the (111) superlattice, mainly because of the fact that the (111)  $\text{Ba}_2\text{NiOsO}_6$  monolayer has a smaller density of the magneto-optically active atoms especially Os atoms than that of the bulk.

Now let us compare the MOKE of the two systems with that of well-known MO materials. The Kerr rotation angles of most  $3d$  transition metals and their compounds seldom exceed  $0.5^\circ$  except, e.g., FePt,  $\text{Co}_2\text{Pt}$  [30], and PtMnSb [31]. Manganese pnictides generally have excellent MO properties. In particular, MnBi films possess a large Kerr rotation angle of  $2.3^\circ$  at 1.84 eV in low temperatures [55, 61]. The famous MO material  $\text{Y}_3\text{Fe}_5\text{O}_{12}$  harbors a Kerr rotation of  $0.23^\circ$  at 2.95 eV. Owing to the strong SOC of  $4d$  and  $5d$  transition metal elements, the large MOKE has also been observed in half-metallic double perovskites containing  $4d$  and  $5d$  elements. Among

these double perovskites, Sr<sub>2</sub>FeWO<sub>6</sub> exhibits a maximum Kerr rotation of 3.87° [6]. On the whole, the Kerr rotation angles of bulk Ba<sub>2</sub>NiOsO<sub>6</sub> and its (111) monolayer are at least comparable to these well-known MO materials.

Figures 8 and 9 show that the Kerr rotation ( $\theta_K$ ) and Kerr ellipticity ( $\varepsilon_K$ ) spectra in both structures resemble, respectively, the real part ( $\sigma_{1xy}$ ) and imaginary part ( $\sigma_{2xy}$ ) of the off-diagonal conductivity element except a reversal of sign. This is not surprising because the Kerr effect and the off-diagonal conductivity element are connected via Eq. (6). Indeed, Eq. (6) indicates that the complex Kerr rotation angle would be linearly related to the  $\sigma_{xy}$  if the longitudinal conductivity ( $\sigma_{xx}$ ) varies smoothly. For the photon energy below 1.0 eV, the complex Kerr rotation angles become unphysically large. This is because the  $\sigma_{xx}$  which is in the denominator of Eq. (6), becomes very small.

The calculated complex Faraday rotation angles for both bulk and (111) monolayer Ba<sub>2</sub>NiOsO<sub>6</sub> are displayed in Fig. 10. The Faraday rotation spectra are rather similar to the corresponding Kerr rotation spectra as well as the  $\sigma_{xy}$  (see Figs. 8 and 9). Figures 7-9 show that the  $\sigma_{xx}$  is generally much larger than the corresponding  $\sigma_{xy}$ . Therefore,  $n_{\pm} = [1 + \frac{4\pi i}{\omega}(\sigma_{xx} \pm i\sigma_{xy})]^{1/2} \approx [1 + \frac{4\pi i}{\omega}\sigma_{xx}]^{1/2} \mp \frac{2\pi}{\omega}(\sigma_{xy}/\sqrt{1 + \frac{4\pi i}{\omega}\sigma_{xx}})$ . Consequently  $\theta_F + i\epsilon_F \approx -\frac{2\pi d}{c}(\sigma_{xy}/\sqrt{1 + \frac{4\pi i}{\omega}\sigma_{xx}})$ , and this explains why the complex Faraday rotation more or less follows  $\sigma_{xy}$  (see Figs. 8, 9, and 10).

Remarkably, the maximum Faraday rotation angles are as large as  $\sim -250$  deg/ $\mu\text{m}$  at  $\sim 3.3$  eV in bulk Ba<sub>2</sub>NiOsO<sub>6</sub> [see Fig. 10(a)] and  $\sim 160$  deg/ $\mu\text{m}$  at 4.1 eV in the monolayer [see Fig. 10(c)]. As mentioned above, manganese pnictides usually have excellent MO properties, and among them MnBi films possess the largest Faraday rotations of  $\sim 80.0$  deg/ $\mu\text{m}$  at 1.77 eV at low temperatures [55, 61]. However, the famous MO material Y<sub>3</sub>Fe<sub>5</sub>O<sub>12</sub> possesses only a moderate Faraday rotation of 0.19 deg/ $\mu\text{m}$  at 2.07 eV. By substituting Y with Bi, Vertruyen *et al.* obtained an enhanced Faraday rotation of  $\sim 35.0$  deg/ $\mu\text{m}$  at 2.76 eV Bi<sub>3</sub>Fe<sub>5</sub>O<sub>12</sub> [62]. Also as mentioned above, large magnetooptical effects are observed in some half-metallic double perovskites containing 4d and 5d transition metals. For example, Sr<sub>2</sub>FeWO<sub>6</sub> possesses a large Faraday rotation of 45.0 deg/ $\mu\text{m}$  [6]. Clearly, the Faraday rotation angles in both bulk Ba<sub>2</sub>NiOsO<sub>6</sub> and its (111) monolayer are larger than these well-known MO materials. Therefore, because of their excellent MO properties, these Ba<sub>2</sub>NiOsO<sub>6</sub> materials could find promising applications for, e.g., MO sensors and high density MO data-storage devices.

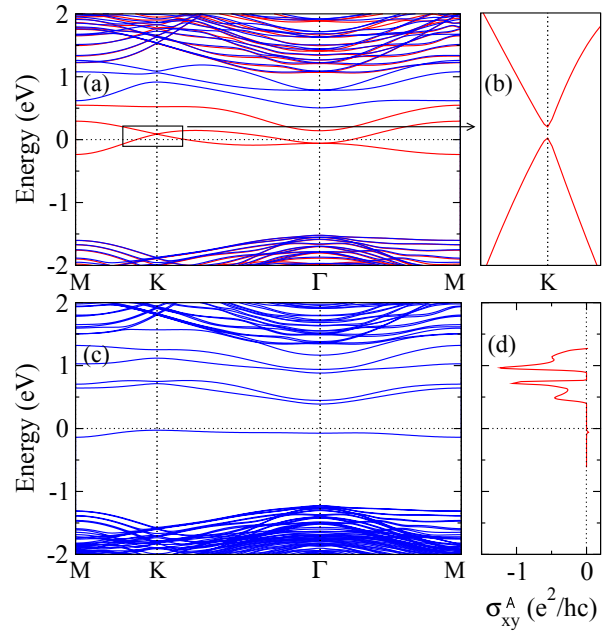


FIG. 11: (a) Scalar-relativistic and (c) relativistic band structures as well as (d) anomalous Hall conductivity ( $\sigma_{xy}^A$ ) of the (111) Ba<sub>2</sub>NiReO<sub>6</sub> monolayer. The part in the box in (a) is enlarged and displayed in (b). The FM magnetization is along the *c*-axis and the Fermi level is at 0 eV.

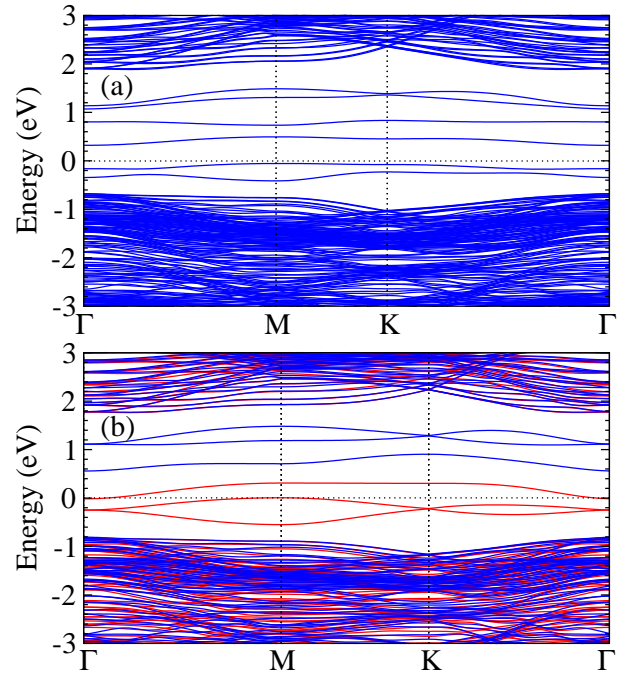


FIG. 12: (a) Fully-relativistic and (b) scalar-relativistic band structures of the (111) Ba<sub>2</sub>NiOsO<sub>6</sub> monolayer. The Fermi level is at 0 eV. In panel (b), red and blue curves represent up-spin and down-spin bands, respectively.

### E. Anomalous Hall conductivity and topological phases

As mentioned before, bulk  $\text{Ba}_2\text{NiOsO}_6$  and its (111) superlattice are found to be FM semiconductors when the SOC is included. We thus could expect that the band gap would be topologically nontrivial and they could be Chern insulators. To verify the topological nature of this insulating gap, we calculate the anomalous Hall conductivity (AHC) ( $\sigma_{xy}^A$ ) for the two structures. For a three-dimensional (3D) quantum Hall insulator,  $\sigma_{xy}^A = n e^2/hc$ , where  $c$  is the lattice constant along the  $c$  axis normal to the plane of longitudinal and Hall currents and  $n$  is an integer known as the Chern number ( $n_C$ ) [63, 64]. For a normal FM insulator, however,  $\sigma_{xy}^A = 0$ . The calculated AHC of bulk  $\text{Ba}_2\text{NiOsO}_6$  and its (111) superlattice are displayed in Figs. 4(b) and 4(d), respectively. Unfortunately,  $\sigma_{xy}^A$  is zero within the band gap in both systems, that is, the gaps are topologically trivial and they are just normal FM insulators.

Here our design principle for engineering topological insulators is to find a material with its scalar-relativistic band structure that possesses Dirac points in the BZ, and then examine whether an energy gap would be opened at these Dirac points when the SOC is turned-on. For bulk  $\text{Ba}_2\text{NiOsO}_6$ , an ideal cubic perovskite structure, the Ni and Os ions sit on a simple cubic lattice with the Ni  $3d$  or Os  $5d$  orbitals being split into twofold degenerate  $e_g$  and threefold degenerate  $t_{2g}$  levels by the octahedral crystal-field. However, such a lattice geometry usually does not support Dirac points, as one can see from the calculated scalar-relativistic band structure in Fig. 5(a). This explains that bulk  $\text{Ba}_2\text{NiOsO}_6$  remains topologically trivial when the SOC is switched-on. Recently, Xiao et al. discovered [39] that in a metallic (111)  $\text{ABO}_3$  perovskite bilayer, in which TM B ions form a buckled honeycomb lattice [see, e.g., Fig. 1(c)], the TM B  $e_g$  and  $t_{2g}$  bands would form Dirac points at the K point in the BZ. As a result, when the SOC is switched-on, a topologically nontrivial energy gap would be opened at the Dirac points and hence the system would be a topological insulator. Indeed, it has been subsequently demonstrated by many researchers (see, e.g., Refs. [40–42] and references therein) that the topological phase can be achieved in either a (111) simple perovskite bilayer or a (111) double-perovskite monolayer. In the (111)  $\text{Ba}_2\text{NiOsO}_6$  monolayer, Ni and Os ions form a honeycomb lattice [see, e.g., Fig. 1(c)], and thus Dirac points appear at the K point below the Fermi level [Fig. 5(b)]. Therefore, when the SOC is turned-on, the energy gap opened at the Dirac point is topologically nontrivial [see Fig. 4(b)]. Nevertheless, we have also calculated the relativistic band structure for the (001)  $\text{Ba}_2\text{NiOsO}_6$  monolayer. As expected, the (001) monolayer is a topologically trivial metal.

Interestingly, the calculated  $\sigma_{xy}^A$  in (111)  $\text{Ba}_2\text{NiOsO}_6$  superlattice is  $2.0 e^2/hc$  within the band gap opened at these Dirac points with the SOC turned on [Fig. 4(d)], i.e., the band gap is topologically nontrivial. Therefore,

within the rigid band model, one may speculate that the quantum anomalous Hall phase would appear in the (111)  $\text{Ba}_2\text{NiOsO}_6$  superlattice when doped with one hole. There are several ways of hole doping such as chemical substitution [65] and electrostatic gating [66, 67]. Here we explore both the chemical substitution and electrostatic gating. Specifically, we first consider three kinds of chemical substitutions, namely, replacing one  $\text{Ba}^{2+}$  ion with an alkali metal ( $X = \text{Li, Na, K}$ ) atom as  $\text{BaXNiOsO}_6$ , replacing the  $\text{Ni}^{2+}$  ion with a transition metal ( $Y = \text{Sc, Mn, Co, Cu, Ru}$ ) atom as  $\text{Ba}_2\text{YO}_6$ , and also substitution of  $\text{Re}^{6+}$  for  $\text{Os}^{6+}$ . Unfortunately, the resultant band structures for the second kind of substitutions are all metallic. For the first and third kinds of substitutions, the resultant compounds are semiconductors. Nonetheless, the semiconducting gaps are all topologically trivial, i.e.,  $\sigma_{xy}^A$  is zero within the band gap. As an example, we display the calculated scalar-relativistic and relativistic band structures as well as AHC ( $\sigma_{xy}^A$ ) of the (111)  $\text{Ba}_2\text{NiReO}_6$  superlattice in Fig. 11. Figure 11(d) shows clearly that the  $\sigma_{xy}^A$  of the  $\text{Ba}_2\text{NiReO}_6$  superlattice is zero within the semiconducting gap. We note that the intersection at the K point near the Fermi level does not exist even without the SOC [Fig. 11 (b)]. This may explain why the (111)  $\text{Ba}_2\text{NiReO}_6$  superlattice is topologically trivial. We also simulate the hole doping by electrostatic gating. Here, we perform self-consistent electronic structure calculations with one less valence electron per f.u. Unfortunately, the resultant band structure becomes metallic, indicating that the rigid band model is inapplicable here because of too strong perturbation due to the hole doping.

## IV. CONCLUSIONS

In conclusion, by performing systematic first-principles density functional calculations, we have investigated magnetism, electronic structure, magneto-optical effects and topological property of cubic double perovskite  $\text{Ba}_2\text{NiOsO}_6$  and its (111)  $(\text{Ba}_2\text{NiOsO}_6)_1/(\text{BaTiO}_3)_{10}$  monolayer superlattice. Interestingly, we find that both structures are rare FM semiconductors, and the ferromagnetism is driven by strong FM coupling between neighboring Ni and Os atoms, which in turn arises from the FM superexchange mechanism due to the abnormally strong hybridization between half-filled Ni  $e_g$  and unoccupied Os  $e_g$  orbitals. The strong SOC on the Os atom not only opens the semiconducting gap but also results in a large negative orbital magnetic moment on the Os atom, thus leading to a total magnetic moment ( $3.37 \mu_B/\text{f.u.}$ ) of less than  $4.0 \mu_B/\text{f.u.}$  [12], expected from the  $\text{Ni}^{2+} 3d^8 (t_{2g}^6 e_g^2; S = 1)$  and  $\text{Os}^{6+} 5d^2 (t_{2g}^2 e_g^0; S = 1)$  ions. We also find that because of the enhanced effective intra-atomic exchange splitting of the Os atoms caused by the Ni  $3d$  - Os  $5d$  hybridization and the strong SOC on the Os sites,  $\text{Ba}_2\text{NiOsO}_6$  exhibits large MO effects. In particular, the Kerr and Faraday rotations can be as large as

TABLE III: Calculated total and atomic spin ( $m_s$ ) and orbital ( $m_o$ ) magnetic moments as well as band gap ( $E_g$ ) of bulk  $\text{Ba}_2\text{NiOsO}_6$  as a function of effective on-site Coulomb repulsions  $U_{Os}$  and  $U_{Ni}$  in the GGA + U + SOC method.

$U_{Os}$ (eV)	$U_{Ni}$ (eV)	$m_s^{Os}$ ( $\mu_B/\text{atom}$ )	$m_s^{Ni}$ ( $\mu_B/\text{atom}$ )	$m_o^s$ ( $\mu_B/\text{f.u.}$ )	$m_o^s$ ( $\mu_B/\text{atom}$ )	$m_o^{Ni}$ ( $\mu_B/\text{atom}$ )	$m_o^o$ ( $\mu_B/\text{f.u.}$ )	$m_s^{tot}$ ( $\mu_B/\text{f.u.}$ )	$m_o^{tot}$ ( $\mu_B/\text{f.u.}$ )	$E_g$ (eV)
1	3	1.155	1.712	0.681	-0.505	0.195	-0.079	3.738	-0.368	0.0
1	4	1.150	1.746	0.650	-0.505	0.205	-0.079	3.732	-0.359	0.0
1	5	1.142	1.779	0.621	-0.505	0.217	-0.078	3.725	-0.346	0.0
2	3	1.232	1.710	0.672	-0.547	0.196	-0.085	3.771	-0.413	0.2
2	4	1.229	1.744	0.642	-0.549	0.205	-0.084	3.768	-0.405	0.2
2	5	1.224	1.777	0.614	-0.550	0.211	-0.083	3.764	-0.399	0.2
3	3	1.314	1.708	0.655	-0.570	0.197	-0.086	3.793	-0.435	0.4
3	4	1.312	1.743	0.624	-0.571	0.206	-0.085	3.791	-0.427	0.4
3	5	1.308	1.776	0.597	-0.572	0.216	-0.084	3.789	-0.416	0.4

$6^\circ$  and  $250 \text{ deg}/\mu\text{m}$ , respectively, which are much larger than that of best-known MO materials. For the  $(111)$   $(\text{Ba}_2\text{NiOsO}_6)_1/(\text{BaTiO}_3)_{10}$  superlattice, a large Kerr rotation of  $\sim 2^\circ$  and a large Faraday rotation of about  $160 \text{ deg}/\mu\text{m}$  is also predicted, although they are smaller than that bulk  $\text{Ba}_2\text{NiOsO}_6$ , mainly due to the reduced density of magneto-optically active atoms especially Os atoms in the superlattice. These theoretical findings therefore suggest that cubic double perovskite  $\text{Ba}_2\text{NiOsO}_6$  and its  $(111)$  superlattice are excellent materials for not only semiconductor-based spintronics but also magneto-optical devices. Finally, the calculated AHC reveals that the band gap just below the Fermi level in the monolayer superlattice is topologically nontrivial with the gap Chern number of 2 although both structures are ordinary FM semiconductors. This indicates that the  $(111)$   $\text{Ba}_2\text{NiOsO}_6$  and related  $5d$  double-perovskite monolayers may provide an interesting material platform for exploring magnetic topological phases and phase transitions. This work is thus expected to stimulate further experimental and theoretical investigations on these interesting materials.

### Acknowledgments

The authors acknowledge support from the Ministry of Science and Technology, National Center for Theoretical Sciences, and Academia Sinica of the Republic of China. H.-S.L. is also supported by the National Natural Science Foundation of China under Grant No. 11704046.

### Appendix A: GGA+U+SOC calculations

The calculated spin, orbital, and total magnetic moments for Ni and Os atoms as well as band gap for bulk  $\text{Ba}_2\text{NiOsO}_6$  from GGA + U + SOC are listed in Table III. Clearly, the Coulomb repulsion  $U$  on both atoms has little effect on the calculated magnetic moments. However, the Coulomb repulsion  $U$  at Os site ( $U_{Os}$ ) plays an essential role in opening the band gap, and the band gap increases with  $U_{Os}$ . The obtained band gap agrees

TABLE IV: Symmetry adapted Ni and Os basis functions of the  $O_h$  point group at  $\Gamma$  for bulk  $\text{Ba}_2\text{NiOsO}_6$ .  $E$  denotes the degeneracy of the band states.

Symmetry	$E$	Basis functions
$\Gamma_{1+}$ ( $\Gamma_1, A_{1g}$ )	1	$s$
$\Gamma_{3+}$ ( $\Gamma_{12}, E_g$ )	2	$x^2 - y^2, 2z^2 - x^2 - y^2$
$\Gamma_{4+}$ ( $\Gamma'_{15}, T_{1g}$ )	3	$xy(x^2 - y^2), yz(y^2 - z^2), zx(z^2 - x^2)$
$\Gamma_{5+}$ ( $\Gamma'_{25}, T_{2g}$ )	3	$xy, yz, zx$
$\Gamma_{2-}$ ( $\Gamma'_2, A_{2u}$ )	1	$xyz$
$\Gamma_{4-}$ ( $\Gamma_{15}, T_{1u}$ )	3	$x, y, z$
$\Gamma_{5-}$ ( $\Gamma_{25}, T_{2u}$ )	3	$z(x^2 - y^2), x(y^2 - z^2), y(z^2 - x^2)$

TABLE V: Symmetry adapted Ni and Os basis functions of the  $C_{3v}$  point group at  $\Gamma$  for the  $(\text{Ba}_2\text{NiOsO}_6)_1/(\text{BaTiO}_3)_{10}$  superlattice.  $E$  denotes the degeneracy of the band states.

Symmetry	$E$	Basis functions
$\Gamma_1$ ( $A_1$ )	1	$z; x^2 + y^2; z^2$
$\Gamma_2$ ( $A_2$ )	1	$R_z$
$\Gamma_3$ ( $E$ )	2	$x, y; x^2 - y^2, xy; xz, yz; R_x, R_y$

well with published experimental value of  $0.31 \text{ eV}$  when  $U_{Os}$  ranging from  $2.0$  to  $3.0 \text{ eV}$ . Therefore, the effective Coulomb repulsions  $U_{Os} = 2.0 \text{ eV}$  and  $U_{Ni} = 5.0 \text{ eV}$  are adopted in this paper.

### Appendix B: Band structure of $(111)$ $\text{Ba}_2\text{NiOsO}_6$ monolayer superlattice

The full band structure of the  $(111)$   $\text{Ba}_2\text{NiOsO}_6$  monolayer superlattice is displayed in Fig. 12(a) (with SOC) and Fig. 12(b) (no SOC). The corresponding band structure with only the monolayer-dominated bands being displayed, is given in Figs. 4(b) and 5(b), respectively.

### Appendix C: Symmetry analysis

Bulk  $\text{Ba}_2\text{NiOsO}_6$  has the space group  $Fm\bar{3}m$  with its point group  $O_h$  having 48 symmetry operations. The

TABLE VI: Dipole selection rules between the band states of point group  $O_h$  at  $\Gamma$ . Relationships between the single group and double group representations are:  $\Gamma_1^+ \rightarrow \Gamma_6^+$ ;  $\Gamma_3^+ \rightarrow \Gamma_5^+, \Gamma_8^+$ ;  $\Gamma_4^+ \rightarrow \Gamma_5^+, \Gamma_6^+, \Gamma_7^+, \Gamma_8^+$ ;  $\Gamma_5^+ \rightarrow \Gamma_6^+, \Gamma_7^+, \Gamma_8^+$ ;  $\Gamma_2^- \rightarrow \Gamma_7^-$ ;  $\Gamma_4^- \rightarrow \Gamma_5^-, \Gamma_6^-, \Gamma_7^-, \Gamma_8^-$ ;  $\Gamma_4^- \rightarrow \Gamma_5^-, \Gamma_6^-, \Gamma_7^-, \Gamma_8^-$ . [69]

	$E \perp c \ \& \ E \parallel c$
Single group	$\Gamma_{1+} \longleftrightarrow \Gamma_{4-}$ $\Gamma_{3+} \longleftrightarrow \Gamma_{4-}, \Gamma_{5-}$ $\Gamma_{4+} \longleftrightarrow \Gamma_{1-}, \Gamma_{3-}, \Gamma_{4-}, \Gamma_{5-}$ $\Gamma_{5+} \longleftrightarrow \Gamma_{2-}, \Gamma_{3-}, \Gamma_{4-}, \Gamma_{5-}$ $\Gamma_{2-} \longleftrightarrow \Gamma_{5+}$ $\Gamma_{4-} \longleftrightarrow \Gamma_{1+}, \Gamma_{3+}, \Gamma_{4+}, \Gamma_{5+}$ $\Gamma_{5-} \longleftrightarrow \Gamma_{2+}, \Gamma_{3+}, \Gamma_{4+}, \Gamma_{5+}$
Double group	$\Gamma_{1+} \longleftrightarrow \Gamma_{4-}$ $\Gamma_{3+} \longleftrightarrow \Gamma_{4-}, \Gamma_{5-}$ $\Gamma_{4+} \longleftrightarrow \Gamma_{1-}, \Gamma_{3-}, \Gamma_{4-}, \Gamma_{5-}$ $\Gamma_{5+} \longleftrightarrow \Gamma_{2-}, \Gamma_{3-}, \Gamma_{4-}, \Gamma_{5-}$ $\Gamma_{2-} \longleftrightarrow \Gamma_{5+}$ $\Gamma_{4-} \longleftrightarrow \Gamma_{1+}, \Gamma_{3+}, \Gamma_{4+}, \Gamma_{5+}$ $\Gamma_{5-} \longleftrightarrow \Gamma_{2+}, \Gamma_{3+}, \Gamma_{4+}, \Gamma_{5+}$

TABLE VII: Dipole selection rules between the band states of point group  $C_{3v}$  at  $\Gamma$ . Relationships between the single group and double group representations are:  $\Gamma_1 \rightarrow \Gamma_5, \Gamma_6$ ;  $\Gamma_1 \rightarrow \Gamma_5, \Gamma_6$ ;  $\Gamma_3 \rightarrow \Gamma_4, \Gamma_5, \Gamma_6$ . [69]

	$E \perp c$	$E \parallel c$
Single group	$\Gamma_1 \longleftrightarrow \Gamma_3$ $\Gamma_2 \longleftrightarrow \Gamma_3$ $\Gamma_3 \longleftrightarrow \Gamma_1, \Gamma_2, \Gamma_3$	$\Gamma_1 \longleftrightarrow \Gamma_1$ $\Gamma_2 \longleftrightarrow \Gamma_2$ $\Gamma_3 \longleftrightarrow \Gamma_3$
double group	$\Gamma_1 \longleftrightarrow \Gamma_3$ $\Gamma_2 \longleftrightarrow \Gamma_3$ $\Gamma_3 \longleftrightarrow \Gamma_1, \Gamma_2, \Gamma_3$	$\Gamma_1 \longleftrightarrow \Gamma_1$ $\Gamma_2 \longleftrightarrow \Gamma_2$ $\Gamma_3 \longleftrightarrow \Gamma_3$

site-symmetry point group for Ni and Os atoms is also  $O_h$ .  $(111)(\text{Ba}_2\text{NiOsO}_6)_1/(\text{BaTiO}_3)_{10}$  monolayer superlattice, however, has the space group  $P3ml$  with its point group  $C_{3v}$  including six symmetry operations. The site-symmetry point group for Ni and Os atoms is  $C_{3v}$ . To determine the symmetry of the band states at the center ( $\Gamma$ -point) of the Brillouin zone (BZ), the symmetry adapted basis functions, formed from the atomic orbitals localized at the Ni and Os sites, are derived using the projection method of group theory [68], as listed in Tables V and VI for the  $O_h$  and  $C_{3v}$  point groups, respectively. By comparing the calculated orbital characters of the band states at the  $\Gamma$ -point with the symmetry-adapted basis functions (Tables V and VI), one can determine the symmetries of the  $\Gamma$ -point band states for bulk  $\text{Ba}_2\text{NiOsO}_6$  and its  $(\text{Ba}_2\text{NiOsO}_6)_1/(\text{BaTiO}_3)_{10}$  superlattice, as shown in Figs. 4 and 5.

Given the known symmetries of the band states at a  $k$ -point in the BZ, the possible direct inter-band transitions can be worked out using the dipole selection rules. The dipole selection rules for the  $O_h$  and  $C_{3v}$  point groups [69] are listed in Tables VI and VII, respectively. Using these selection rules, we assign the prominent peaks in the optical conductivity (Figs. 7, 8 and 9) of bulk  $\text{Ba}_2\text{NiOsO}_6$  and its  $(\text{Ba}_2\text{NiOsO}_6)_1/(\text{BaTiO}_3)_{10}$  superlattice to the principal inter-band transitions at the  $\Gamma$  point, as shown in Figs. 4 and 5.

- [1] A. W. Sleight and R. Ward, J. Am. Chem. Soc. **83**, 1088 (1961).  
[2] K. I. Kobayashi, T. Kimura, H. Sawada, K. Terakura, and Y. Tokura, Nature (London) **395**, 677 (1998).  
[3] M. Azuma, K. Takata, T. Saito, S. Ishiwata, Y. Shimakawa, and M. Takano, J. Am. Chem. Soc. **127**, 8889 (2005).  
[4] H. T. Jeng and G. Y. Guo, Phys. Rev. B **67**, 094438 (2003).  
[5] J. B. Philipp, P. Majewski, L. Alff, A. Erb, R. Gross, T. Graf, M. S. Brandt, J. Simon, T. Walther, W. Mader, D. Topwal, and D. D. Sarma, Phys. Rev. B **68**, 144431 (2003).  
[6] R. Vidya, P. Ravindran, A. Kjekshus, and H. Fjellvåg, Phys. Rev. B **70**, 184414 (2004).  
[7] H. Das, M. D. Raychaudhury, and T. Saha-Dasgupta, Appl. Phys. Lett. **92**, 201912 (2008).  
[8] A. M. Cook and A. Paramakanti, Phys. Rev. Lett. **113**, 077203 (2014).  
[9] A. M. Cook, Phys. Rev. B **94**, 205135 (2016).  
[10] H. Zhang, H. Huang, K. Hauke, and D. Vanderbilt, Phys. Rev. B **90**, 165143 (2014).  
[11] X.-Y. Dong, S. Kanungo, B. Yan and C.-X. Liu, Phys. Rev. B **94**, 245135 (2016).  
[12] H. L. Feng, S. Calder, M. P. Ghimire, Y. H. Yuan, Y. Shirako, Y. Tsujimoto, Y. Matsushita, Z. Hu, C.-Y. Kuo, L. H. Tjeng, T.-W. Pi, Y.-L. Soo, J. He, M. Tanaka, Y. Katsuya, M. Richter, and K. Yamaura, Phys. Rev. B **94**, 235158 (2016).  
[13] Y. K. Wang and G. Y. Guo, Phys. Rev. B **73**, 064424 (2006).  
[14] Y. K. Wang, P. H. Lee and G. Y. Guo, Phys. Rev. B **80**, 224418 (2009).  
[15] P. M. Oppeneer, Chapter 1 Magneto-optical Kerr Spectra, pp. 229-422, in *Handbook of Magnetic Materials*, edited by K. H. J. Buschow. Elsevier, Amsterdam, (2001).  
[16] V. Antonov, B. Harmon, and A. Yaresko, Electronic Structure and Magneto-Optical Properties of Solids (Kluwer Academic, Dordrecht, 2004).  
[17] C. Gong, L. Li, Z. Li, H. Ji, A. Stern, Y. Xia, T. Cao, W. Bao, C. Wang, Y. Wang, Z. Q. Qiu, R. J. Cava, S. G. Louie, J. Xia and X. Zhang, Nature **546**, 265 (2017).  
[18] B. Huang, G. Clark, E. Navarro-Moratalla, D. R. Klein, R. Cheng, K. L. Seyler, D. Zhong, E. Schmidgall, M. A. McGuire, D. H. Cobden, W. Yao, D. Xiao, P. Jarillo-

- Herrero, X. Xu, *Nature* **546**, 270–273 (2017).
- [19] Y. Fang, S. Wu, Z.-Z. Zhu and G.-Y. Guo, *Phys. Rev. B* **98**, 125416 (2018).
- [20] C. Stamm, C. Murer, M. Berritta, J. Feng, M. Gabureac, P. M. Oppeneer, P. Gambardella, *Phys. Rev. Lett.* **119**, 087203 (2017).
- [21] W. Jiang, X. Zhang, G. Yu, W. Zhang, X. Wang, M. B. Jungfleisch, J. E. Pearson, X. Cheng, O. Heinonen, K. L. Wang, Y. Zhou, A. Hoffmann and S. G. E. te Velthuis, *Nat. Phys.* **13**, 162 (2017).
- [22] A. Lehnert, S. Dennler, P. Bloński, S. Rusponi, M. Etzkorn, G. Moulas, P. Bencok, P. Gambardella, H. Brune, and J. Hafner, *Phys. Rev. B* **82**, 094409 (2010).
- [23] W. He, H.-L. Liu, H.-Y. Wu, J.-W. Cai, and Z.-H. Cheng, *Appl. Phys. Lett.* **106**, 042401 (2015).
- [24] W.-K. Tse and A. H. MacDonald, *Phys. Rev. Lett.* **105**, 057401 (2010).
- [25] R. Valdes Aguilar, A. V. Stier, W. Liu, L. S. Bilbro, D. K. George, N. Bansal, L. Wu, J. Cerne, A. G. Markelz, S. Oh, and N. P. Armitage, *Phys. Rev. Lett.* **108**, 087403 (2012).
- [26] M. Mansuripur, *The Physical Principles of Magneto-Optical Recording* (Cambridge University, New York, 1995).
- [27] P. N. Argyres, *Phys. Rev.* **97**, 334 (1955).
- [28] J. L. Erskine and E. A. Stern, *Phys. Rev. Lett.* **30**, 1329 (1973).
- [29] J. L. Erskine and E. A. Stern, *Phys. Rev. B* **8**, 1239 (1973).
- [30] G. Y. Guo and H. Ebert, *J. Magn. Magn. Mater.* **156**, 173 (1996).
- [31] P. G. van Engen, K. H. J. Buschow, R. Jongebreur, and M. Erman, *Appl. Phys. Lett.* **42**, 202 (1983).
- [32] D. D. Sarma, P. Mahadevan, T. Saha-Dasgupta, S. Ray, and A. Kumar, *Phys. Rev. Lett.* **85**, 2549 (2000).
- [33] J. Kanamori and K. Terakura, *J. Phys. Soc. Jpn.* **70**, 1433 (2001).
- [34] J. Mannhart and D. G. Schlom, *Science* **327**, 1607 (2010).
- [35] H. Y. Hwang, Y. Iwasa, M. Kawasaki, B. Keimer, N. Nagaosa, and Y. Tokura, *Nat. Mater.* **11**, 103 (2012).
- [36] A. Ohtomo and H. Y. Hwang, *Nature (London)* **427**, 423 (2004).
- [37] P.-W. Lee, V. N. Singh, G. Y. Guo, H.-J. Liu, J.-C. Lin, Y.-H. Chu, C. H. Chen, and M.-W. Chu, *Nat. Commun.* **7**, 12773 (2016).
- [38] H.-S. Lu, T.-Y. Cai, S. Ju, and C.-D. Gong, *Phys. Rev. Applied* **3**, 034011 (2015).
- [39] D. Xiao, W. Zhu, Y. Ran, N. Nagaosa, and S. Okamoto, *Nat. Commun.* **2**, 596 (2011).
- [40] H. K. Chandra, and G. Y. Guo, *Phys. Rev. B* **95**, 134448 (2017).
- [41] H. S. Lu, and G. Y. Guo, *Phys. Rev. B* **99**, 104405 (2019).
- [42] S. Baidya, U. V. Waghmare, A. Paramakanti, and T. SahaDasgupta, *Phys. Rev. B* **94**, 155405 (2016).
- [43] See Supplemental Material for Tables S1 and S2, which includes Ref. [12].
- [44] J. P. Perdew, K. Burke, and M. Ernzerhof, *Phys. Rev. Lett.* **77**, 3865 (1996).
- [45] P. E. Blöchl, *Phys. Rev. B* **50**, 17953 (1994).
- [46] G. Kresse and J. Hafner, *Phys. Rev. B* **47**, 558 (1993); G. Kresse and J. Furthmüller, *Phys. Rev. B* **54**, 11169 (1996).
- [47] S. L. Dudarev, G. A. Botton, S. Y. Savrasov, C. J. Humphreys and A. P. Sutton, *Phys. Rev. B* **57**, 1505 (1998).
- [48] F. Wooten, *Optical Properties of Solids* (Academic, New York, 1972).
- [49] C. S. Wang and J. Callaway, *Phys. Rev. B* **9**, 4897 (1974).
- [50] B. Adolph, J. Furthmüller and F. Bechstedt, *Phys. Rev. B* **63**, 125108 (2001).
- [51] W. M. Temmerman, P. A. Sterne, G. Y. Guo and Z. Szotek, *Molecular Simulations* **63**, 153 (1989).
- [52] H. S. Bennett and E. A. Stern, *Phys. Rev.* **137**, A448 (1965).
- [53] G. Y. Guo and H. Ebert, *Phys. Rev. B* **50**, 10377 (1994).
- [54] G. Y. Guo and H. Ebert, *Phys. Rev. B* **51**, 12633 (1995).
- [55] P. Ravindran, A. Delin, P. James, B. Johansson, J. M. Wills, R. Ahuja, and O. Eriksson, *Phys. Rev. B* **59**, 15680 (1999).
- [56] D. Xiao, M.-C. Chang, and Q. Niu, *Rev. Mod. Phys.* **82**, 1959 (2010).
- [57] X. Wang, J. R. Yates, I. Souza, and D. Vanderbilt, *Phys. Rev. B* **74**, 195118 (2006).
- [58] M. G. Lopez, D. Vanderbilt, T. Thonhauser, and I. Souza, *Phys. Rev. B* **85**, 014435 (2012).
- [59] N. Marzari, A. A. Mostofi, J. R. Yates, I. Souza, and D. Vanderbilt, *Rev. Mod. Phys.* **84**, 1419 (2012).
- [60] J. B. Goodenough, *Phys. Rev.* **100**, 564 (1955); J. Kanamori, *J. Phys. Chem. Solids* **10**, 87 (1959).
- [61] G. Di and S. Uchiyama, *Phys. Rev. B* **53**, 3327 (1996).
- [62] B. Vertruyen, R. Cloots, J. S. Abell, T. J. Jackson, R. C. da Silva, E. Popova and N. Keller, *Phys. Rev. B* **78**, 094429 (2008).
- [63] B. I. Halperin, *Jpn. J. Appl. Phys.* **26**, 1913 (1987).
- [64] J. Zhou, Q.-F. Liang, H. Weng, Y. B. Chen, S.-H. Yao, Y.-F. Chen, J. Dong and G.-Y. Guo, *Phys. Rev. Lett.* **116**, 256601 (2016).
- [65] M. P. Ghimire and M. Richter, *Nano Lett.* **17**, 6303 (2017).
- [66] B. Huang, G. Clark, D. R. Klein, D. MacNeill, E. Navarro-Moratalla, K. L. Seyler, N. Wilson, M. A. McGuire, D. H. Cobden, D. Xiao, W. Yao, P. Jarillo-Herrero and X. Xu, *Nature Nanotechn.* **13**, 544 (2018).
- [67] S. Jiang, L. Li, Z. Wang, K. F. Mak and J. Shan, *Nature Nanotechn.* **13**, 549 (2018).
- [68] M. S. Dresselhaus, G. Dresselhaus, and A. Jorio, *Group Theory: Application to the Physics of Condensed Matter*, (Springer, New York, 2007).
- [69] W. Eberhardt, F. J. Himpsel, *Phys. Rev. B* **21**, 5572 (1980).